

# Topological Signals of Singularities in Ricci Flow

Paul M. Alsing<sup>\*1</sup>, Howard A. Blair<sup>†2</sup>, Matthew Corne<sup>‡3</sup>, Gordon Jones<sup>§4</sup>,  
 Warner A. Miller<sup>¶5</sup>, Konstantin Mischaikow<sup>||6</sup>, and Vudit Nanda<sup>\*\*7</sup>

<sup>1</sup>Air Force Research Laboratory, Information Directorate, Rome, NY 13441

<sup>2</sup>Department of Electrical Engineering and Computer Science, Syracuse University, Syracuse, NY 13244

<sup>3</sup>Department of Mathematics, Statistics, and Computer Science, University of Wisconsin–Stout, Menomonie, WI 54751

<sup>4</sup>Wolverine Trading, LLC, Chicago, IL 60604

<sup>5</sup>Department of Physics, Florida Atlantic University, Boca Raton, FL 33431

<sup>6</sup>Department of Mathematics, Rutgers University, Piscataway, NJ 08854

<sup>7</sup>Department of Mathematics, University of Pennsylvania, Philadelphia, PA 19104

## Abstract

We apply the methods of persistent homology to investigate singularity formation in a selection of geometries evolved numerically by Ricci flow. To implement persistent homology, we construct a triangular mesh for a sample of points. The scalar curvature along the edges of the triangulation, computed as an average of scalar curvatures at the endpoints of the edges, serves as a filtration parameter at each time step. We analyze the topological signals of geometric criticality obtained from the application of persistent homology to a two-dimensional rotational solid that collapses to a round point and three-dimensional dumbbells that manifest neckpinch singularities under Ricci flow and show that these signals are distinct. Finally, we discuss the interpretation and implication of these results and future applications.

## 1 Introduction

Persistent homology (PH) [6, 12, 18, 24] is a method of topological data analysis (TDA). It is useful for analyzing data generated by nonlinear processes. Examples include data sets not amenable to a linear fit, a collection of data points representing some surface or manifold, or information for which a suitable metric is unknown or not easily specified.

Hamilton’s Ricci flow (RF) [16] is a system of partial differential equations (PDE’s) that has been used in the classification of two and three dimensional geometries [9, 26] via the uniformization

---

<sup>\*</sup>paul.alsing@us.af.mil

<sup>†</sup>blair@ecs.syr.edu

<sup>‡</sup>cornem@uwstout.edu

<sup>§</sup>gojones@umich.edu

<sup>¶</sup>wam@fau.edu

<sup>||</sup>mischaik@math.rutgers.edu

<sup>\*\*</sup>vnanda@sas.upenn.edu

theorem and geometrization conjecture, respectively. Of interest is the formation of singularities [2, 3, 14] in the solutions of the RF equations. In two dimensions, compact surfaces with 2-sphere topology collapse to round points while in three dimensions, a finite number of pinching singularities can occur in different parts of the geometry, depending on the problem being considered.

The goal of this work is to capture, via PH, a topological signal – specifically, the Betti number spectra, tables measuring lengths of persistence intervals, and distances between persistence diagrams – of the formation of critical geometric phenomena in RF. This provides a quantitative method for identifying common trends in the resulting collection of data obtained by solution of these PDE’s. Even with a complete set of data and methods for collection and measurement, numerical simulations typically limit us to pointwise snapshots at single moments of time of quantities of interest. Also, such simulations are plagued with stiffness that obstructs or distorts the evolution of a system. Persistent homology provides a method for evaluating an entire collection of and tracking trends in data across an entire domain of interest and at each step of the time evolution by identifying whether multiple small effects or fewer large effects dominate changes in the geometry. In the particular case of the numerical solution of RF, one would like to capture the process of diffusion of curvature on the manifold at different resolutions and to see whether or not this diffusion is occurring through changes in multiple small features or through changes in fewer large features over time in the collection of points. The motivation for applying PH to RF is for a potential synthesis of techniques from topology and geometry in various applications including imaging, networks, and quantum entanglement.

In Section 2, we review the necessary mathematical preliminaries. These include brief expositions of persistent homology, Ricci flow, and singularity formation in RF. In Section 3, we describe the models, our data-generating algorithm, the initial and boundary conditions for the different models, the assignment of the data to a triangulation, and the algorithm used to acquire the topological signals of the models. In Section 4, we present the analysis of the models. Our results show that PH provides distinct topological signals for the models when uniformization occurs, when collapse occurs, or when a singularity is encountered. We conclude with Section 5, where we review the results and discuss their interpretation and implication. Finally, we present future applications.

## 2 Preliminaries and Background

We begin with summaries of **persistent homology** and **Ricci flow**. Since our treatment of these topics is cursory, we refer the interested reader to [6, 12, 13, 24] for overviews of persistent homology and its applications and to [20, 21] for various technical details pertaining to Ricci flow and its discrete analogues.

### 2.1 Persistent Homology

A *filtration* consists of a one-parameter family of triangulable topological spaces  $X_p$  indexed by some real number  $p \in \mathbb{R}$  subject to the constraint that  $X_p$  is a subspace of  $X_q$  whenever  $p \leq q$ . At its core, persistent homology associates to each filtration a sequence of intervals  $[b_*, d_*]$ , called *persistence intervals* or *lifespans*, which are indexed by homology classes across all of the  $X_p$ ’s as  $p$  ranges from  $-\infty$  to  $\infty$ . Here we describe how those intervals are obtained in the special case where each intermediate topological space in the filtration is a finite simplicial complex  $\mathcal{K}_p$ . For the purposes of this section, we do not require an ambient Euclidean space containing all of the simplicial complexes – it suffices to assume finiteness and the subcomplex relation  $\mathcal{K}_p \hookrightarrow \mathcal{K}_q$  whenever  $p \leq q$ .

**Definition 2.1.** Given a simplicial filtration  $\{\mathcal{K}_p \mid p \in \mathbb{R}\}$ , the  $d$ -dimensional  $\ell$ -persistent homology group of  $\mathcal{K}_p$  is the image of the map  $H_d(\mathcal{K}_p) \rightarrow H_d(\mathcal{K}_{p+\ell})$  induced on (ordinary) homology groups by the inclusion of  $\mathcal{K}_p$  into  $\mathcal{K}_{p+\ell}$ .

In general, even the space of simplicial filtrations is too large for persistent homology groups to provide a useful invariant, so one adds a local finiteness assumption as follows. A simplicial filtration  $\{\mathcal{K}_p \mid p \in \mathbb{R}\}$  is said to be *tame* whenever the set of indices  $p$  for which the inclusion  $\mathcal{K}_{p-\epsilon} \hookrightarrow \mathcal{K}_{p+\epsilon}$  does *not* induce an isomorphism on homology for all dimensions is finite. Henceforth we will assume that all filtrations are tame.

One may compute homology with coefficients in a field to obtain, for each simplicial filtration  $\{\mathcal{K}_p\}$  and for each dimension  $d \geq 0$ , a one-parameter family of vector spaces  $\{H_d(\mathcal{K}_p)\}$  which comes equipped with linear maps  $\phi_{p \rightarrow q} : H_d(\mathcal{K}_p) \rightarrow H_d(\mathcal{K}_q)$  whenever  $p \leq q$ . These maps are induced on homology by including  $\mathcal{K}_p$  into  $\mathcal{K}_q$  and therefore satisfy the associative property: the composite  $H_d(\mathcal{K}_p) \rightarrow H_d(\mathcal{K}_q) \rightarrow H_d(\mathcal{K}_r)$  is the same as  $H_d(\mathcal{K}_p) \rightarrow H_d(\mathcal{K}_r)$  across any increasing triple  $p \leq q \leq r$  of positive real numbers. Such a family of vector spaces and linear maps is called a *persistence module*.

Two key results involving persistence modules make persistent homology an ideal candidate for investigating the topological changes in a filtered space. The first has to do with a finite representation. Associated to any interval<sup>1</sup>  $[a, b]$  with  $b \geq a$  is the *interval module*  $\mathbf{I}_{[a,b]}$  whose constituent vector spaces are trivial whenever  $p \notin [a, b]$  and one-dimensional otherwise; the linear maps are identities whenever the source and target vector spaces are both nontrivial. The following proposition was first proved in [28] and has been substantially generalized since [7].

**Proposition 2.2.** Every persistence module arising from a tame simplicial filtration is canonically isomorphic to a direct sum of **interval modules**.

In particular, the isomorphism classes of persistence modules are conveniently indexed by a finite family of intervals of the form  $[a, b]$ . The  $d$ -dimensional *persistence diagram* (hereafter PD) of a tame simplicial filtration  $\{\mathcal{K}_p\}$  is defined to be the collection of intervals which arise from the decomposition of its  $d$ -dimensional persistence module.

The second key result confers robustness to persistent homology and is usually called the **stability theorem** [7]. The basic idea is that the space of all simplicial filtrations and the space of persistence diagrams (hereafter PD's) may both be assigned natural metric structures so that the process of associating to each filtration its PD's is 1-Lipschitz.

## 2.2 Ricci Flow

Let  $\mathcal{M}$  be a smooth compact Riemannian manifold with metric  $\mathbf{g}$ . Let  $\Xi(\mathcal{M})$  be the set of vector fields on  $\mathcal{M}$ . Then, the *Riemann curvature tensor* is the tensor  $\mathbf{Rm} : \Xi(\mathcal{M}) \times \Xi(\mathcal{M}) \times \Xi(\mathcal{M}) \rightarrow \Xi(\mathcal{M})$  given by

$$R(X, Y, Z) = \nabla_X \nabla_Y Z - \nabla_Y \nabla_X Z - \nabla_{[X, Y]} Z \quad (1)$$

where  $\nabla_U V$  is the covariant derivative of  $V$  with respect to the vector field  $U$  [4, 22]. The Riemann tensor measures the difference between the resulting vectors obtained at a point  $q \in \mathcal{M}$  by parallel transporting a vector along two different paths starting at a point  $p \in \mathcal{M}$ .

Ricci flow (RF) is a geometric flow that evolves the metric  $\mathbf{g}$  on  $\mathcal{M}$  by the equation

$$\frac{d}{dt} \mathbf{g} = -2 \mathbf{Ric}, \quad (2)$$

---

<sup>1</sup>We allow semi-infinite intervals here, so the right endpoint is allowed to equal  $\infty$ .

where the  $\cdot$  indicates differentiation with respect to an external time parameter,  $t$ . The Ricci tensor  $\mathbf{Ric}$  is a contraction of the Riemann tensor  $\mathbf{Rm}$  – producing a tensor of type  $(0, 2)$  from a tensor of type  $(1, 3)$  – and provides a certain average of the sectional curvatures of all 2–planes along a given direction. It was introduced in the early 1980’s by R. Hamilton [5, 16].

The RF equation (2) yields a forced diffusion equation for the scalar curvature  $R$  so that it evolves as

$$\dot{R} = \Delta R + 2 |\mathbf{Ric}|^2 \quad (3)$$

and tends to uniformly distribute curvature over the manifold. Here,  $\Delta_g$  is the usual Beltrami–Laplace operator with respect to the metric, and  $|\cdot|$  is the tensor norm.

In three and higher dimensions, RF can develop singularities in curvature. For 3–dimensional manifolds, such flows can admit a finite number of these singularities at distinct times in the interval  $t \in [0, \infty)$ . Identifying, understanding, and surgically removing these singularities was an essential step in Hamilton’s program and Perelman’s proof of Thurston’s geometrization conjecture to decompose a manifold into its prime and simple pieces [9].

### 2.2.1 Singularities in Ricci Flow

We review the work of [9, 16, 17]. Consider a solution  $(\mathcal{M}, g(t))$  of RF which exists on a maximal time interval  $[0, T)$ . Such a solution is *maximal* if  $|\mathbf{Rm}|$  – where  $\mathbf{Rm}$  is the Riemann tensor – is unbounded as  $t \rightarrow T$ ,  $T < \infty$  or  $T = \infty$ . If  $T < \infty$  and  $|\mathbf{Rm}|$  becomes unbounded as  $t \rightarrow T$ , then a maximal solution develops singularities, and  $T$  is called the *singularity time* [14].

There exist several types of singularities.

**Definition 2.3.** [8] *Let  $(\mathcal{M}, g(t))$  be a solution of RF that exists up to a maximal time  $T \leq \infty$ . We say a solution to the RF develops a*

1. **Type–I singularity** at a maximal time  $T < \infty$  if

$$\sup_{t \in [0, T)} (T - t) \max\{|\mathbf{Rm}(x, t)| : x \in \mathcal{M}\} < \infty;$$

2. **Type–IIa singularity** at a maximal time  $T < \infty$  if

$$\sup_{t \in [0, T)} (T - t) \max\{|\mathbf{Rm}(x, t)| : x \in \mathcal{M}\} = \infty;$$

3. **Type–IIb singularity** at a maximal time  $T < \infty$  if

$$\sup_{t \in [0, \infty)} \max\{|\mathbf{Rm}(x, t)| : x \in \mathcal{M}\} = \infty;$$

4. **Type–III singularity** at a maximal time  $T < \infty$  if

$$\sup_{t \in [0, \infty)} \max\{|\mathbf{Rm}(x, t)| : x \in \mathcal{M}\} < \infty.$$

The dumbbells investigated in this work will form two kinds of “neckpinch” singularities: non-degenerate and degenerate. An example of a nondegenerate neckpinch was established in [3]. We review the notation and some necessary definitions [2].

**Definition 2.4.** A sequence  $\{(x_j, t_j)\}_{j=0}^{\infty}$  of points and times in a RF solution is called a **blow-up sequence at time  $T$**  if  $t_j \rightarrow T$  and if  $|\mathbf{Rm}(x_j, t_j)| \rightarrow \infty$  as  $j \rightarrow \infty$ .

Such a sequence has a corresponding pointed singularity model if the sequence of parabolic dilation metrics  $\mathbf{g}_j(x, t) := |\mathbf{Rm}(x_j, t_j)|\mathbf{g}(x, t_j + |\mathbf{Rm}(x_j, t_j)|^{-1}t)$  has a complete smooth limit.

**Definition 2.5.** Given a RF solution  $(\mathcal{M}, \mathbf{g}(t))$ , a **neckpinch singularity** develops at a time  $T$  if there is some blow-up sequence at  $T$  whose corresponding pointed singularity model exists and is given by the self-similarly shrinking Ricci soliton on the cylinder  $\mathbb{R} \times S^n$ .

## 3 Methodology

### 3.1 Models

We investigate topological signals of singularity formation for a dimpled sphere on  $S^2$  and dumbbells on  $S^3$  in this work. The types of dumbbells include a small-lobed symmetric dumbbell, a dimpled dumbbell (“genetically modified peanut” [3]), and a degenerate dumbbell [14]. Singularity formation in such examples is well-understood [2, 3, 9, 14].

The “dimpled” sphere is modeled by a metric whose radial function depends on the polar angle  $\theta$  and time and is given by

$$\mathbf{g}(t) = r^2(\theta, t)\mathbf{g}_{can} \quad (4)$$

where  $\mathbf{g}_{can} = d\theta^2 + \sin^2 \theta d\phi^2$  is the canonical metric on a 2-sphere. The angular measures are usually  $-\pi/2 < \theta < \pi/2$  (polar) and  $0 \leq \phi < 2\pi$  (azimuthal). For our algorithm, it is convenient to modify the polar angle so that  $0 < \theta < \pi$ ; this is the angle over which we construct the initial radial profile  $r(\theta, 0)$ .

By the uniformization theorem [16], any 2–geometry will evolve under RF to a constant curvature sphere, plane, or hyperboloid. Regarding singularity formation, this will lead to the collapse of a sphere to a round point, and the dimpled sphere will Ricci flow to a sphere of constant curvature before collapsing to a round point. The shrinking round sphere is a Type-I singularity.

The dumbbells are constructed by puncturing  $S^3$  at the poles  $\{N, S\}$  and identifying  $S^3 \setminus \{N, S\}$  with  $(-c, c) \times S^2$  where  $c$  is a constant usually taken as 1. This identification is for convenience to avoid working in multiple patches [2]. Letting  $x$  denote the coordinate on  $(-c, c)$  and  $\mathbf{g}_{can}$  denote the canonical unit sphere metric on  $S^2$ , an arbitrary family  $\mathbf{g}(t)$  of smooth  $SO(3)$ –invariant metrics on  $S^3$  may be written in geodesic polar coordinates as

$$\mathbf{g}(t) = \varphi^2(x, t)dx^2 + \psi^2(x, t)\mathbf{g}_{can}. \quad (5)$$

The function  $\psi^2(x, t)$  is a “radial” function for the profile of the dumbbell with one dimension suppressed. This manifests as corseting of the dumbbell.

An alternative representation of this metric – the warped product metric – is to introduce a geometric coordinate which normalizes the metric in the variable associated with the interval and leaves only a radial function present [3]. The distance from the “equator”  $\{0\} \times S^n$  is given by

$$s(x, t) = \int_0^x \varphi(x', t)dx'. \quad (6)$$

It follows that  $\partial s / \partial x = \varphi(x, t)$ , and this changes the metric to

$$\mathbf{g}(t) = ds^2 + \psi^2(s, t)\mathbf{g}_{can}. \quad (7)$$

We formulate an initial-value and boundary-value problem for each of the dumbbells; this is achieved conveniently by considering both  $\varphi(x, t)$  and  $\psi(x, t)$ , so we use (5). The initial and boundary conditions for the radial function  $\psi(x, t)$  of the dumbbells depend on the model. We use Neumann conditions on the boundaries to satisfy the requirements for the values of the derivatives on approaching the poles [3],

$$\lim_{x \rightarrow \pm c} \frac{\partial \psi}{\partial s} = \mp 1, \quad (8)$$

which can be expressed in terms of  $x$  since  $(\partial x / \partial s)|_{t=0} = 1/\varphi(x, 0)$ . The boundary conditions at the poles are necessary such that the metric on the dumbbell extends smoothly to a metric on  $S^3$ .

The dumbbells, under RF, will manifest neckpinch singularities. These come in two types: *non-degenerate* and *degenerate*.

**Definition 3.1.** A neckpinch singularity is **nondegenerate** if every pointed singularity model of any blow-up sequence corresponding to  $T$  is a cylindrical solution. The following are basic assumptions in [2] for such singularity formation in  $SO(n+1)$ -invariant solutions of RF with an initial set of data of the form (7):

1. The sectional curvature  $L$  of planes tangent to each sphere  $\{s\} \times S^n$  is positive.
2. The Ricci curvature  $\mathbf{Rc} = nKds^2 + [K + (n-1)L]\psi^2\mathbf{g}_{can}$  (where  $K$  is the sectional curvature of a plane orthogonal to  $\{s\} \times S^n$ ) is positive on each polar cap.
3. The scalar curvature  $R = 2nK + n(n-1)L$  is positive everywhere.
4. The metric has at least one neck and is “sufficiently pinched” in the sense that the value of the radial function  $\psi$  at the smallest neck is sufficiently small relative to its value at either adjacent bump.
5. The metric is reflection symmetric, and the smallest neck is at  $x = 0$ .

Here,

$$\begin{aligned} L &= \frac{1 - \psi_s^2}{\psi^2} = \frac{1 - (\psi_x/\varphi)^2}{\psi^2}, \quad \text{and} \\ K &= -\frac{\psi_{ss}}{\psi} = -\frac{(-\varphi_x\psi_x/\varphi^2 + \psi_{xx}/\varphi)}{\varphi\psi}. \end{aligned} \quad (9)$$

Nondegenerate neckpinches are Type-I singularities.

An obvious consequence of the positivity of the tangential sectional curvature  $L$  is that  $|\psi_s| \leq 1$ . This makes construction of suitable models more challenging and places constraints on any randomized construction.

We will now discuss degenerate neckpinches.

**Definition 3.2.** *A neckpinch singularity is **degenerate** if there is at least one blow-up sequence at  $T$  with a pointed singularity model that is not a cylindrical solution. The basic assumptions in [2] for an open set of initial data are as follows for degenerate neckpinches:*

1. *The solutions of RF are  $SO(n+1)$ -invariant such that criteria (1) - (3) in Def. 3.1 for non-degenerate neckpinches hold.*
2. *The initial data may have at least one neck or no necks (hence degenerate dumbbells [14]).*
3. *It is assumed that a singularity occurs at the “right” pole ( $x = +1$ ) at some time  $T < \infty$ .*

To investigate degenerate neckpinches, we exploit the following Lemma [14]:

**Lemma 3.3.** *Suppose  $g_\alpha(t)$ , with parameter  $\alpha \in [0, 1]$ , is a rotationally symmetric solution of the RF on  $S^{n+1}$  with  $g_\alpha(0) = \varphi^2(x, 0)dx^2 + \psi_\alpha^2(x, 0)g_{can}$ ,  $x \in [-1, 1]$ . If, at initial, the scalar curvature  $R^{(\alpha)} > 0$ ,  $\psi_\alpha(x, 0)$  has only one bump, is nonincreasing on the right polar cap and strictly concave on the left polar cap, and  $|\partial\psi_\alpha/\partial s|(x, 0) \leq 1$  on  $[-1, 1]$ , then either the solution  $g_\alpha(t)$  develops a Type-II singularity or it shrinks to a round point.*

## 3.2 Persistence Computations

Consider a triangulated manifold  $\mathcal{K}$  of dimension  $n$  such that each  $d$ -dimensional simplex  $\sigma$  has been assigned a real number  $\iota(\sigma)$ . From this data, one can construct a filtration  $\{\mathcal{K}_p \mid p \geq 0\}$  compatible with  $\iota$  such that for each  $\sigma$  in  $\mathcal{K}$  of dimension  $d$ ,

$$\inf \{p \in \mathbb{R} \mid \sigma \in \mathcal{K}_p\} = \iota(\sigma).$$

That is, the smallest value of  $p$  for which a given  $d$ -simplex  $\sigma$  lies in  $\mathcal{K}_p$  is required to equal  $\iota(\sigma)$ . There are various ad-hoc ways to extend  $\iota$ -values to simplices of dimensions other than  $d$  so that a compatible filtration may be imposed on  $\mathcal{K}$ . A more principled route is via the *star filtration* which has been used, for instance, in the persistent homological analysis of image data [25].

**Definition 3.4.** *Given a triangulated  $n$ -manifold  $\mathcal{K}$  and a real-valued function  $\iota$  defined on the  $d$ -simplices for some  $0 \leq d \leq n$ , the **star filtration** along  $\iota$  is defined via the following containment relation for each  $p \in \mathbb{R}$  and each simplex  $\sigma \in \mathcal{K}$ : we have  $\sigma \in \mathcal{K}_p$  if and only if one of the following conditions holds:*

- $\dim \sigma < d$  and there is some  $d$ -dimensional co-face  $\tau \succ \sigma$  with  $\iota(\tau) \geq p$ , or
- $\dim \sigma = d$  and  $\iota(\sigma) \leq p$ , or
- $\dim \sigma > d$  and there is some  $d$ -dimensional face  $\tau \prec \sigma$  with  $\iota(\tau) \leq p$ .

The extreme cases  $d = 0$  and  $d = n$  are called upper and lower star filtrations. To construct a star filtration, consider a simplex in  $\mathcal{K}$ . If its dimension equals  $d$ , then its filtration index equals its  $\iota$ -value. If its dimension exceeds  $d$ , then it inherits the largest  $\iota$ -value encountered among its  $d$ -dimensional faces. Finally, if its dimension is smaller than  $d$ , then it inherits the smallest  $\iota$  value encountered among all  $d$ -dimensional simplices in  $\mathcal{K}$  which contain this simplex as a face. Note that in order for such a construction to be well-defined, each simplex of dimension smaller than  $d$  must have at least one  $d$ -dimensional co-face. But since we work entirely with triangulated manifolds, this condition is automatically satisfied.

The following describes our methodology for analyzing RF with PH. We begin with a triangulated surface  $\mathcal{K}^0$  evolving via RF with the resulting complexes being labeled  $\mathcal{K}^t$  for some discrete indices  $t \geq 0$ :

1. for each  $\mathcal{K}^t$ , compute curvature values assigned to all vertices,
2. construct the upper star filtration along these values,
3. produce the corresponding PD's in dimensions 0 and 1,
4. instead of birth-death pairs  $(b, d)$ , restrict attention to the differences  $d - b$ , called *persistence intervals* or *lifespans*.

The superscript, associated to discrete time, distinguishes from the subscript, associated with the filtration. **Perseus** [23] generates a reduced complex  $\mathcal{K}'^t$  out of the input simplicial complex  $\mathcal{K}^t$ . The output files depend on the dimension of  $\mathcal{K}'^t$ , which is less than or equal to the dimension of  $\mathcal{K}^t$ . The output files come in two forms at each discrete time step  $t \geq 0$ . One form consists of tables containing persistence intervals for each dimension of  $\mathcal{K}'^t$ . The other form is a table of the *Betti numbers*  $\beta_i$ ,  $i = 0, \dots, n = \dim(\mathcal{K}^t)$ , at each value of the filtration parameter (here, scalar curvature). These numbers provide a count of the number of connected components ( $n = 0$ ) or holes of increasing dimensions ( $n > 0$ ). Then, we plot the lifespans against discretized values of  $t \geq 0$ .

In tandem with the methodology above, we consider PD's – multisets of points in the extended Euclidean plane  $\bar{\mathbb{R}}^2$  [11] – associated with these tables and compute several distance measures between them: bottleneck ( $d_B$ ), Wasserstein-1 ( $d_{W^1}$ ), and Wasserstein-2 ( $d_{W^2}$ ). The *bottleneck distance* is defined as

$$d_B = \inf_{\gamma} \sup_{p \in PD_i} \|p - \gamma(p)\|_{\infty} \quad (10)$$

where  $\gamma : PD_i \rightarrow PD_j$  is a distance-minimizing bijection between PD's, here indexed finitely, and  $\|p - \gamma(p)\|_{\infty} = \max\{|p_x - \gamma(p)_x|, |p_y - \gamma(p)_y|\}$  is the  $L_{\infty}$ -norm on  $\bar{\mathbb{R}}^2$ . For the  $L_{\infty}$ -norm, distances between infinite coordinates are defined to be zero. The *Wasserstein- $q$*  distance is

$$d_{W^q} = \left( \sum_{p \in PD_i} \|p - \gamma(p)\|_{\infty}^q \right)^{1/q}. \quad (11)$$

Note that  $\lim_{q \rightarrow \infty} d_{W^q} = d_B$ . For our system of PD's of finite numbers of points (compared with PD's of continuous functions), in the bottleneck distance, the infimum is a minimum, and the supremum is a maximum.

The bottleneck distance gives an indication of the largest changes in geometry one encounters, while the Wasserstein-1 and -2 distances indicate overall changes in geometry that occur [19].  $d_B$  measures the largest difference between PD's, while  $d_{W^1}$  and  $d_{W^2}$  measure all of the differences

(with  $d_{W^2}$  less sensitive to small changes than  $d_{W^1}$ ). If  $d_{W^1}$  is significantly larger than  $d_B$  and  $d_{W^2}$ , then many small features are responsible for changes in the geometry between PD's. If the distance measures are close, then this indicates a single dominant feature is responsible for changes in the geometry between PD's. For the models, we investigate how the distance measures change over the time evolution of the system. This approach allows us to acquire a persistent homological characterization of the surface – hence a topological signal of its singularity formation – as it undergoes evolution via RF.

### 3.3 Data Generation and Preparation Algorithm

By numerically solving the Ricci flow equations, we compute the scalar curvature. The choices of initial and boundary conditions depend on the particular model.

The initial radial profile for the dimpled sphere with topology  $S^2$  is obtained by constructing a randomized table of values for a collection of angles  $\theta$ . To solve RF, we evolve over the angle  $\theta$  and time. The interval for  $\theta$  is  $[\epsilon, \pi - \epsilon]$  with  $\epsilon = 10^{-3}$ . This choice of interval allows for more stable evolution by reducing potential complications associated with boundary effects.

To obtain a numerical solution in the evolution of the dumbbells – all of which have topology  $(-c, c) \times S^2$  – we approximate the topology of the dumbbells as  $[-c_{Boundary}, c_{Boundary}] \times S^2$ . The endpoints of the closed interval are  $c_{Boundary} = c - \varepsilon$  where  $\varepsilon = \mu\epsilon$ , and  $\mu$  is a scale factor. The endpoints  $\pm c_{Boundary}$  are, variously,  $\pm\mu(\pi/2 - \epsilon)$  (symmetric dumbbell),  $\pm\mu(\pi - \epsilon)$  (dimpled dumbbell), and  $-\mu(\pi/2 - \epsilon)$  on the left pole and another value on the right pole (degenerate dumbbell). For the degenerate dumbbell, the location of the right boundary is determined by the condition that the radial values  $\psi$  match on each pole (i.e., the function is the same height above the  $x$ -axis). We do this because, just by coming in a fixed amount  $\epsilon$  on each pole, we have a difference in radial values in the polar regions.

For all dumbbells, the function  $\varphi(x, t)$  is given initially by  $\varphi(x, 0) = 1$  and at the boundaries by  $\varphi(c_{Boundary}, t) = 1 + t$ . This choice initially satisfies the boundary conditions (8) for  $\psi(x, t)$  on the poles since  $(\partial x / \partial s)|_{t=0} = 1 / \varphi(x, 0) = 1$ .

To address properly the work of [14] (used in Section 4), we need for the initial profile a function, depending on a parameter  $\alpha \in [0, 1]$ , that satisfies the derivative requirements on the poles for the smooth extension of the metric to  $S^3$ ; we impose this on  $g_\alpha(0)$ . Such a function for the initial profile is given by

$$\psi(x, 0) = \frac{-\mu a \left( \frac{x}{\mu} + \frac{\pi}{2} \right) \left( \left( \frac{x}{\mu} - (1 - \alpha)L \right)^2 + h(\alpha, k) \right) \left( \frac{x}{\mu} - \left( \left( \frac{\pi}{2} - L \right) \alpha + L \right) \right)}{(b - \frac{x}{\mu})^{(1-\alpha)}}. \quad (12)$$

We have a freely-specifiable set of parameters  $\{\alpha, L, k, \mu\}$ . The factor  $k$  appears in the definition of  $h(\alpha, k) = -k\alpha + 2k$ ; this function controls the neck thickness. The factor  $(x/\mu - (1 - \alpha)L)^2 + h(\alpha, k)$  controls the position of the neck. We select  $\mu = 100$ , and  $\epsilon = 10^{-3}$ . This choice of  $\mu$  allows for longer time evolution and delay of stiffness due to incrementation limitations. The constants  $a$  and  $b$  depend on the choice of these parameters and are determined by imposing the condition of the derivatives on the poles. The left pole is fixed; the right endpoint is a function of  $\alpha$  and  $L$ ,  $\mu \left( \left( \frac{\pi}{2} - L \right) \alpha + L \right)$ . For dumbbells with  $\alpha \neq 1$ , we adjust the location of the right pole as the radial profile function will otherwise be at a different height above the  $x$ -axis than on the left pole, and we are interested in examining the pinching behavior on the right pole while eliminating artifacts of the construction (i.e., artificial or premature pinching due to closer proximity with the  $x$ -axis than the left pole). So,

we solve for the value on the  $x$ -axis which yields the same radial function value on the right pole as on the left (fixed) pole.

To consider nondegenerate neckpinches satisfying the conditions of [2], we consider a rotationally and reflection symmetric (about the “equator”) dumbbell. This is obtained from (12) with  $\alpha = 1$ . The initial radial profile is a symmetric dumbbell obtained by

$$\psi(x, 0) = -12.6948 \left( \frac{x}{100} + \frac{\pi}{2} \right) \left( \left( \frac{x}{100} \right)^2 + (1/25) \right) \left( \frac{x}{100} - \frac{\pi}{2} \right). \quad (13)$$

The choice of parameters  $L = 1$  and  $k = 1/25$  provides for sufficient pinching. This model satisfies all of the conditions of Definition 3.1.

Interesting topological features occur when the filtration parameter or function has many critical points (e.g., the height function [11]). A way to achieve such a function is to consider the dimpled dumbbell or “genetically modified peanut” [3]. This is an object with multiple necks and multiple bumps. For the dimpled dumbbell, we construct an interpolation function over the interval  $[-100\pi, 100\pi]$ . This interval is larger than for the other dumbbells and is chosen for more stable evolution (though we still come in by 0.1 unit on each pole for the RF computation) and to ease placement of the necks while respecting the derivative conditions for dumbbells.

Motivated by the work of [14], we investigate the profile (12) above with  $\alpha = 0$ . This parameter choice generates a degenerate dumbbell: a dumbbell possessing only one bump and no neck which looks figuratively like an ear dropper. This will allow us, per Lemma 3.3, to investigate whether we have evolution to a Type-II singularity or to a round point. Our initial radial profile is given by

$$\psi(x, 0) = -\frac{15.1309}{1.03112 - x/100} \left( \frac{2}{25} + \left( -1 + \frac{x}{100} \right)^2 \right) \left( -1 + \frac{x}{100} \right) \left( \frac{\pi}{2} + \frac{x}{100} \right). \quad (14)$$

To prepare the data for the PH analysis, we triangulate the manifold in question (Fig. 1). There can be other suitable triangulations of a manifold for numerical evolution of Ricci flow (cf. [20]). For each vertex chosen, we obtain the scalar curvature. To compute the scalar curvature along a given edge of the triangulation, we average the scalar curvatures of the endpoints of the edge. This information is then used to determine scalar curvature values of all edges of the triangulation for each time index. **Perseus** implements this data to compute persistence intervals.

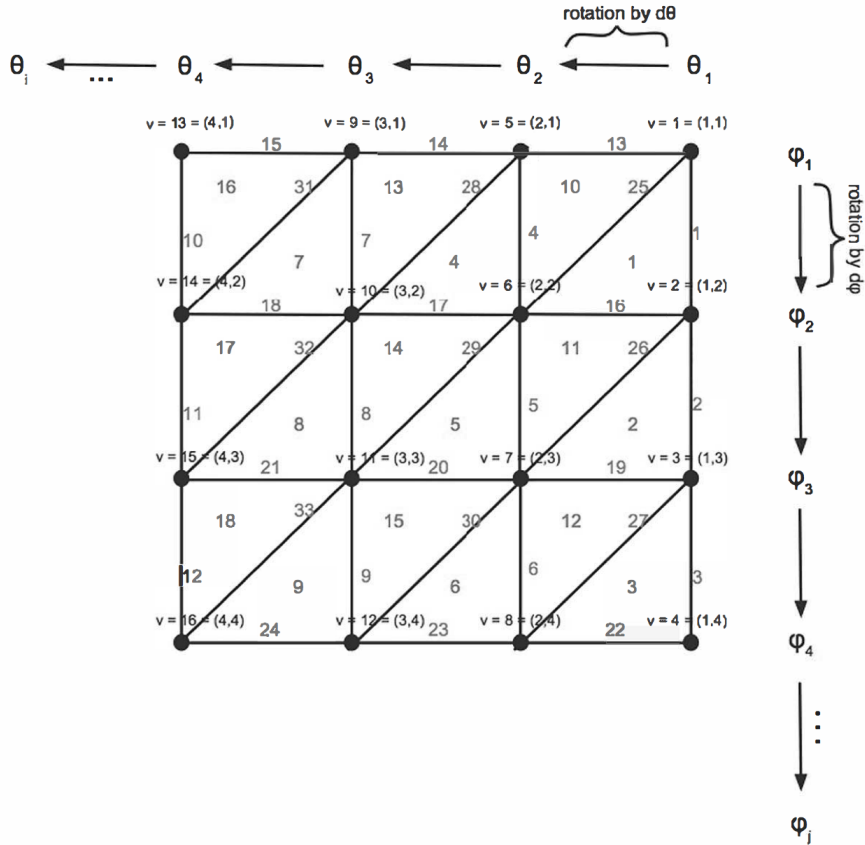


Figure 1: The index  $i$  corresponds with the polar angle  $\theta$ , and the index  $j$  corresponds with the azimuthal angle  $\phi$ . Vertices are indexed as  $(i, j)$  or as the single digit  $v$ , given by  $v = j + (i-1)N\phi$ . The edges are enumerated with blue numbers, and the triangles are enumerated with red numbers. The numbers of points sampled along the directions are given by the notation  $N\theta$  or  $N\phi$ . The increments of angles are computed by  $\Delta\theta = \frac{\pi - 2\varepsilon}{N\theta - 1}$  and  $\Delta\phi = \frac{2\pi}{N\phi - 1}$ .

For all of our models, we can implement the same triangulation. This follows from the symmetry of the dumbbell: in computing the components of the Ricci tensor, the  $\theta\theta$  and  $\phi\phi$  components are redundant so that, out of three, only the  $xx$  and  $\theta\theta$  components need be computed to determine the scalar curvature. The suppression of one of the dimensions of  $S^2$  thus allows the use of a similar triangulation to the dimpled sphere. In the triangulation, the modifications from the dimpled sphere to the dumbbells are  $\theta \rightarrow x$  and

$$\Delta x = 100 \frac{\pi - 2\varepsilon}{Nx - 1}. \quad (15)$$

## 4 Results

First, we plot the initial and final radial profiles for the models. Then, we plot the associated lifespans and investigate the outputs from the different data tables generated by **Perseus**. We refer to these plots and tables in terms of their Betti numbers, so that we have plots and tables associated to  $\beta_0$  (number of connected components) and  $\beta_1$  (number of tunnels). The symmetry of our models means that we have only dimensions 0 and 1. All of the tables for the connected components have a single death value of  $-1$ . This corresponds with the ‘‘first born’’ – lowest birth scalar curvature – and it is the last feature to die. When connected components die, tunnels are born. **Perseus** also outputs a total summary table that, at each time index, goes through an ascending collection of values of the

filtration parameter and indicates the number of connected components and the number of tunnels present for cells born at or below this value. This provides a means to investigate topological signal and noise at *each* time index.

Also, we compute the pairwise distances between adjacent PD's. These distances are the bottleneck, Wasserstein-1, and Wasserstein-2 distances. We plot the adjacent PD's in  $\bar{\mathbb{R}}^2$  that we analyze, selected according to quartile or interesting behavior. Then, the distances between the chosen adjacent PD's are listed in a table, for each Betti number, and provide a characterization of the topological signal. We then compare the values of the distances at different times in the evolution to obtain a quantification of topological signal and noise as we move *across* time indices.

## 4.1 Dimpled Sphere

The rotational solid in Fig. 2 has the topology of  $S^2$  and the appearance of a “dimpled” sphere. The dimpling is obtained by using a random number generator to modulate the initial radius of the solid so that  $r(\theta, 0)$  is an interpolation function built over a table of angles and radii. Ricci flow uniformizes the curvature, transitioning the dimpled sphere to a more conventional-looking sphere which then shrinks to a round point. The triangulation is taken over a  $50 \times 50$  grid for 78 time indices.

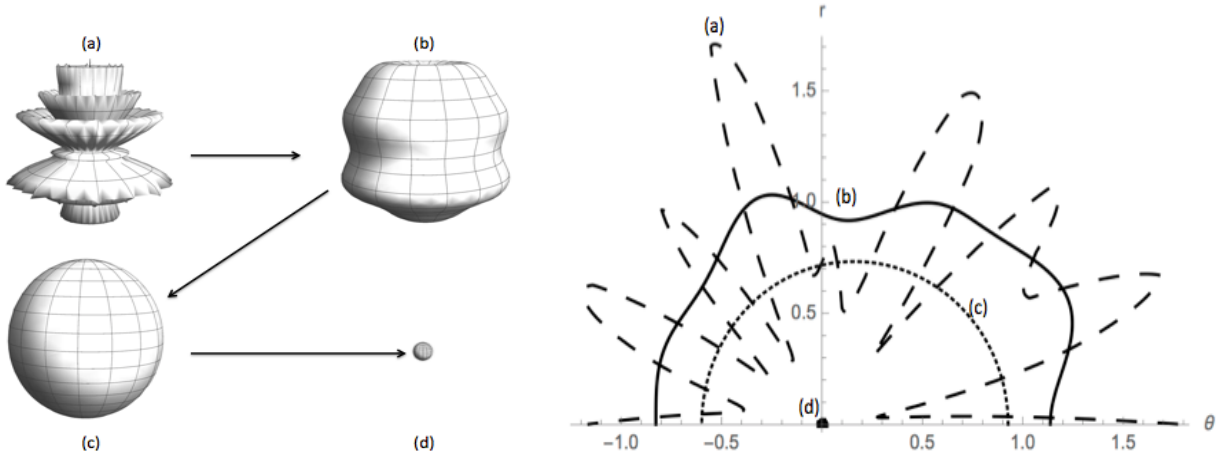


Figure 2: This illustration is of the dimpled sphere and the corresponding radial profiles  $r(\theta, t)$  at time (a)  $t = 0$ ; (b)  $t = 0.03$ ; (c)  $t = 0.3$ ; and (d)  $t = 0.57105$ .

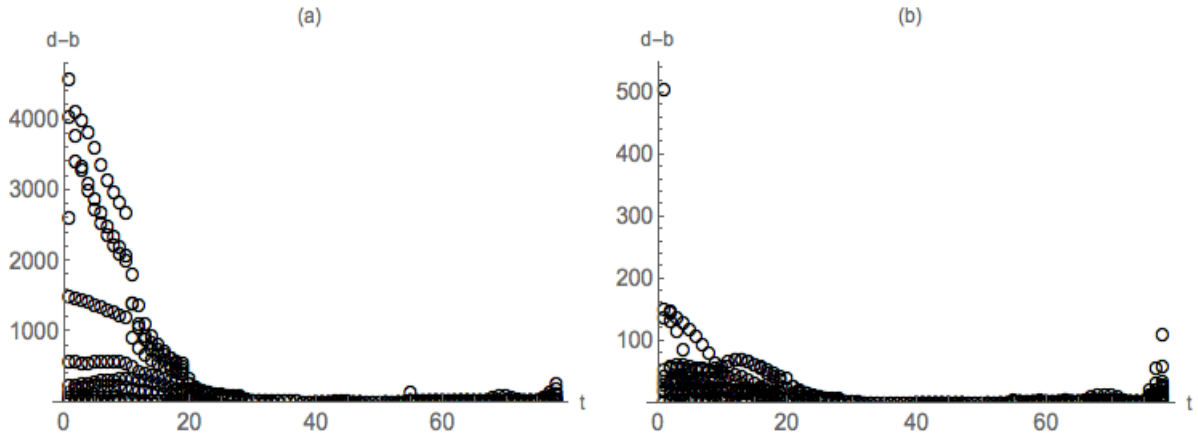


Figure 3: Lifespans ( $d - b$ ) for (a)  $\beta_0$  and (b)  $\beta_1$  computed for  $50 \times 50$  triangulation

Figure 3 features the lifespans  $d - b$  (death - birth) associated to the Betti numbers  $\beta_0$  and  $\beta_1$  versus time index  $t$ . Initially, there are 12 finite lifespans and 1 infinite lifespan associated to the connected components and 12 distinct finite lifespans associated to the holes. This number decreases until, at time index 30000 ( $t = 0.3$ ), there is only one lifespan – of length zero – in the  $\beta_0$  table; this is the first and only time index in the evolution for which only one such lifespan is present. For the  $\beta_1$  table at this time index, there is only a single (distinct) finite interval, also of length zero. In comparing this with the lifespans measured at the first time index, we find that the lifespans have decreased by three orders of magnitude for  $\beta_0$  and two orders of magnitude for  $\beta_1$ . The interpretation is that the scalar curvature throughout the solid has become uniform and begun its collapse. After this, the number of lifespans increases until, at the end of the evolution (when our RF algorithm stiffens), we have 17 finite lifespans and 1 infinite lifespan for the connected components and 17 distinct lifespans for the holes.

In the tables at each time index, we have one connected component and zero holes for the lowest and highest maximum birth scalar curvature with varying numbers of connected components and holes for the scalar curvatures between these values. Also at each time index approaching 30000, the difference between the lowest and highest maximum birth scalar curvatures becomes smaller; this is an indication that the scalar curvature of the object has become uniform. Under RF, it is expected that the dimpling smooths so that the object attains a uniform scalar curvature, then collapses.

We examine the various distance measures in Table 1, focusing attention on the first, last, and some of the PD's between. Approaching the time index where the scalar curvature becomes uniform, the distances all decrease; after this time index, the distances increase again. We can see from the plots of the PD's for the connected components in Figure 4 and holes in Figure 5 that the points in each of the PD's are closer as we approach a uniform value of scalar curvature. Then, they become separated into distinct clusters that are close to the diagonal (green line comprised of equal birth and death values). Given each time index, the adjacent PD's represented by that index have the common feature that  $d_{W^2}$  is closer to  $d_B$  than it is to  $d_{W^1}$ . In Table 2, we examine the ratios  $d_{W^1}/d_B$  and  $d_{W^1}/d_{W^2}$  for both the connected components and holes for the adjacent PD's represented in Table 1. We find that for the first two PD's, the ratios are very close; in comparing this with the lifespans in Figure 3, we see that two of the lifespans are noticeably larger than the others so that some particularly large changes in the geometry dominate differences in the PD's compared with smaller features. This is consistent with the sharp dimpling present in the beginning. But, small features contribute in this case as well and for the rest of the adjacent pairs in Table 1, small changes in the geometry contribute more to differences in the PD compared with a single (large) change. For

the final two diagrams, small features are particularly dominant concerning changes in the geometry. Geometric intuition would suggest that collapse to a round point is a single large effect (thinking in terms of a continuous object) but, as we are looking at a discrete collection of data, and because PH analyzes the data points, this collapse is interpreted in terms of the behavior of the data points. For the discrete data points to collapse to a round point, the points individually must approach a point. Again, looking at the lifespans, at the end of the recorded evolution, we see that the lifespans are increasing but still close in their values. For collapse to a round point, the indication from the topological signal is that the collapse is due to many small features in the data set changing at each time step.

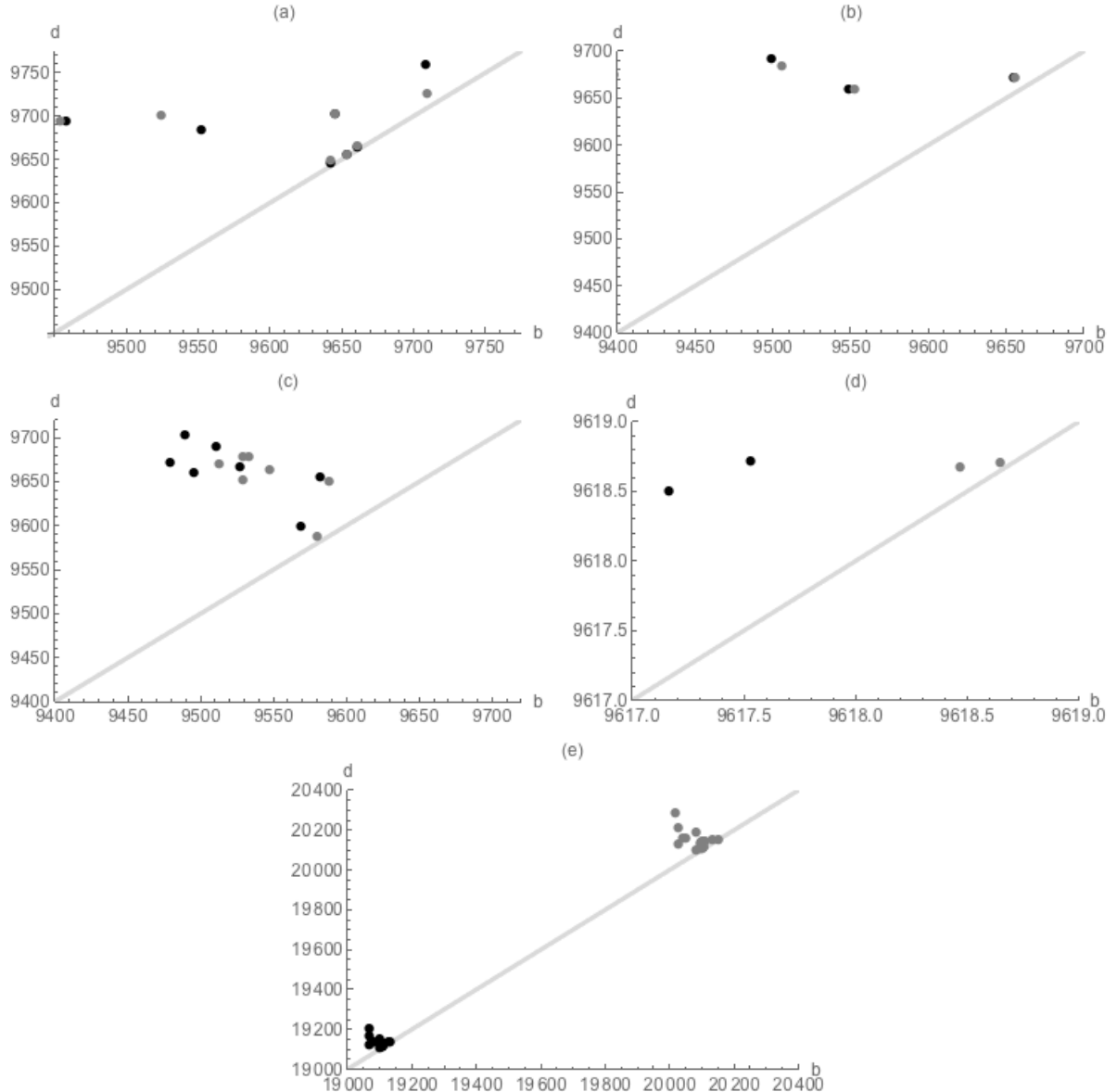


Figure 4: These are plots of the adjacent PD's, death vs. birth ( $d$  vs.  $b$ ), for the connected components ( $\beta_0$ ) for the dimpled sphere represented in the table below where we list the bottleneck, Wasserstein-1, and Wasserstein-2 distances between the adjacent diagrams. We have (a)  $i = 1$ ; (b)  $i = 18$ ; (c)  $i = 21$ ; (d)  $i = 37$ ; (e)  $i = 77$ . The colors of the points in the plots distinguish the time indices from which they come (e.g., black (grey) points are associated with time index  $i$  ( $i+1$ )). The light grey line is the set of points with equal birth and death values. Points related to infinite lifespans are omitted.

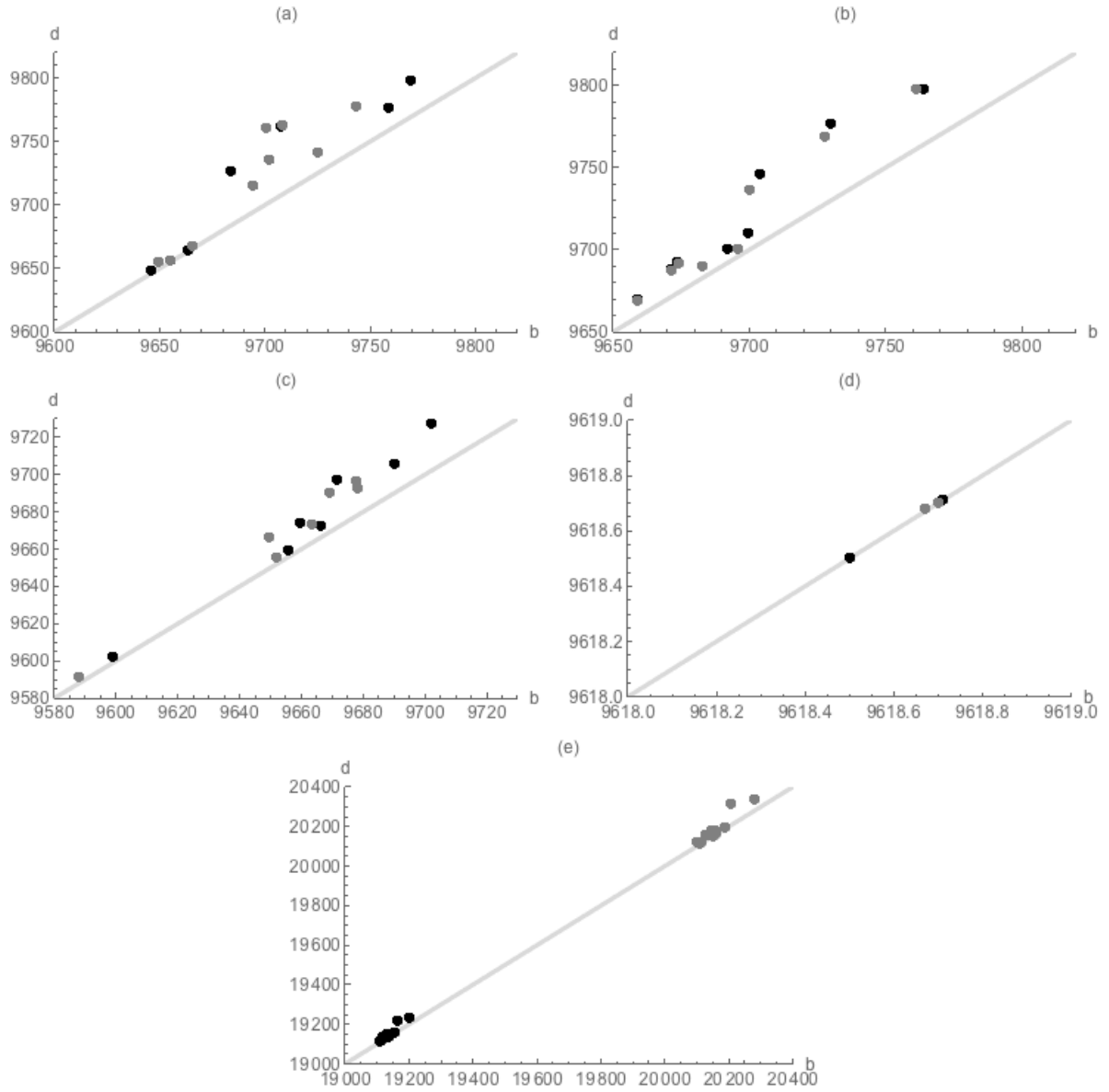


Figure 5: These are plots of the adjacent PD's, death vs. birth ( $d$  vs.  $b$ ), for the connected components ( $\beta_1$ ) for the dimpled sphere represented in the table below where we list the bottleneck, Wasserstein-1, and Wasserstein-2 distances between the adjacent diagrams. We have (a)  $i = 1$ ; (b)  $i = 18$ ; (c)  $i = 21$ ; (d)  $i = 37$ ; (e)  $i = 77$ . The colors of the points in the plots distinguish the time indices from which they come (e.g., black (grey) points are associated with time index  $i$  ( $i+1$ )). The light grey line is the set of points with equal birth and death values. Points related to infinite lifespans are omitted.

Dimpled Sphere	$\beta_0$	$\beta_1$
(PD <sub>i</sub> , PD <sub>i+1</sub> )	(d <sub>B</sub> , d <sub>W1</sub> , d <sub>W2</sub> )	(d <sub>B</sub> , d <sub>W1</sub> , d <sub>W2</sub> )
$i = 1$	( $1.94 \times 10^3$ , $3.46 \times 10^3$ , $2.15 \times 10^3$ )	( $6.95 \times 10^2$ , $8.19 \times 10^2$ , $6.97 \times 10^2$ )
$i = 18$	( $5.42 \times 10^1$ , $2.26 \times 10^2$ , $9.24 \times 10^1$ )	( $1.04 \times 10^1$ , $4.35 \times 10^1$ , $1.93 \times 10^1$ )
$i = 21$	( $3.998 \times 10^1$ , $1.9699 \times 10^2$ , $7.59 \times 10^1$ )	( $3.08 \times 10^1$ , $7.89 \times 10^1$ , $3.76 \times 10^1$ )
$i = 37$	(1.31, 3.73, 2.16)	(0.18, 0.19, 0.1803)
$i = \max$	( $1.08 \times 10^3$ , $1.77 \times 10^4$ , $4.22 \times 10^3$ )	( $1.11 \times 10^3$ , $1.75 \times 10^4$ , $4.24 \times 10^3$ )

Table 1: This table shows the bottleneck, Wasserstein-1, and Wasserstein-2 distances between the first two, middle two, and last two PD's associated with the connected components ( $\beta_0$ ) and holes ( $\beta_1$ ) for the dimpled sphere. There are 78 PD's.

Dimpled Sphere	$\beta_0$	$\beta_1$
(PD <sub>i</sub> , PD <sub>i+1</sub> )	( $d_{W1}/d_B$ , $d_{W1}/d_{W2}$ )	( $d_{W1}/d_B$ , $d_{W1}/d_{W2}$ )
$i = 1$	(1.78, 1.61)	(1.178, 1.175)
$i = 18$	(4.17, 2.45)	(4.18, 2.25)
$i = 21$	(4.93, 2.595)	(2.56, 2.098)
$i = 37$	(2.85, 1.73)	(1.056, 1.054)
$i = \max$	(16.4, 4.19)	(15.8, 4.13)

Table 2: This table shows the ratios ( $d_{W1}/d_B$ ,  $d_{W1}/d_{W2}$ ) of distances between the first two, middle two, and last two PD's associated with the connected components ( $\beta_0$ ) and holes ( $\beta_1$ ) for the dimpled sphere. There are 78 PD's.

## 4.2 Nondegenerate Neckpinch

### 4.2.1 Symmetric Dumbbell

Figure 6 is a plot of the initial and final surfaces, their corresponding neckpinches, and the initial and final radial profiles. The neck radius (at  $x = 0$ ) begins at 1.25293 and ends at 0.00669812, a decrease of three orders of magnitude. The rest of the plot is essentially static with few changes in the values of  $\psi$ . We consider two resolutions for triangulations:  $50 \times 50$  (coarse-grained) and  $100 \times 100$  (finer-grained).

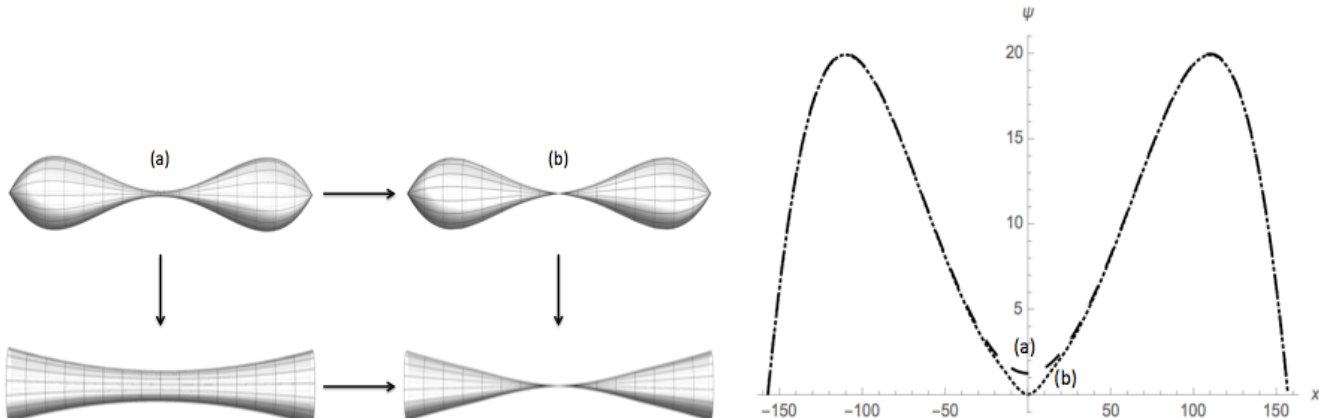


Figure 6: Above are the plots of the symmetric dumbbell at initial time  $t = 0$  and final time  $t = 0.785$ . Below each is a plot of the corresponding neck. The initial and final radial profiles are plotted below these.

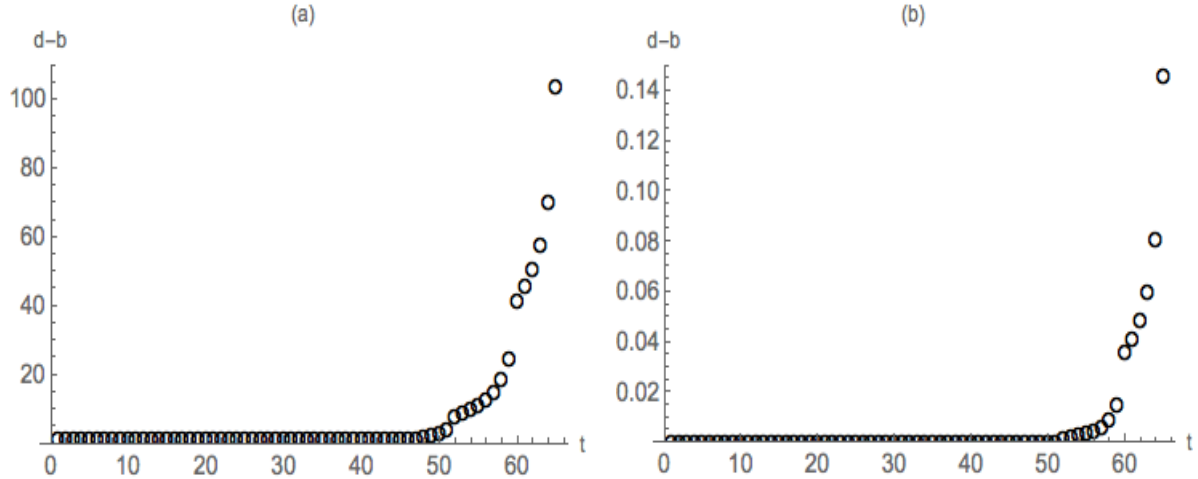


Figure 7: Lifespans  $d - b$  for (a)  $\beta_0$  and (b)  $\beta_1$  computed for  $50 \times 50$  triangulation

For the  $\beta_0$  tables, we have one finite lifespan and one infinite lifespan of low scalar curvature (the infinite lifespan indicates the feature was born first) for all time indices. The lengths of the finite intervals range from 1.1853352 for a birth curvature of 0.0242748 at the first time index to 103.689689 for a birth curvature of 0.0243114 at the final time index. The presence of only a single finite lifespan indicates that we have only one large feature driving the change in curvature of the dumbbell. The  $\beta_1$  tables have multiple lifespans of negligible length. The appearance and disappearance of tunnels indicates that these features are noise related to the filtration process; after we have accounted for all values of curvature, these extraneous features vanish.

Notably, different triangulations capture different curvature features. A coarser triangulation does not capture the high-curvature value for the pinching which occurs at and near the origin for  $\alpha = 1$ . However, comparing coarser ( $50 \times 50$ ) and finer ( $100 \times 100$ ) triangulations, the plots of the lifespans (Fig. 7 and Fig. 8, respectively) appear almost self-similar.

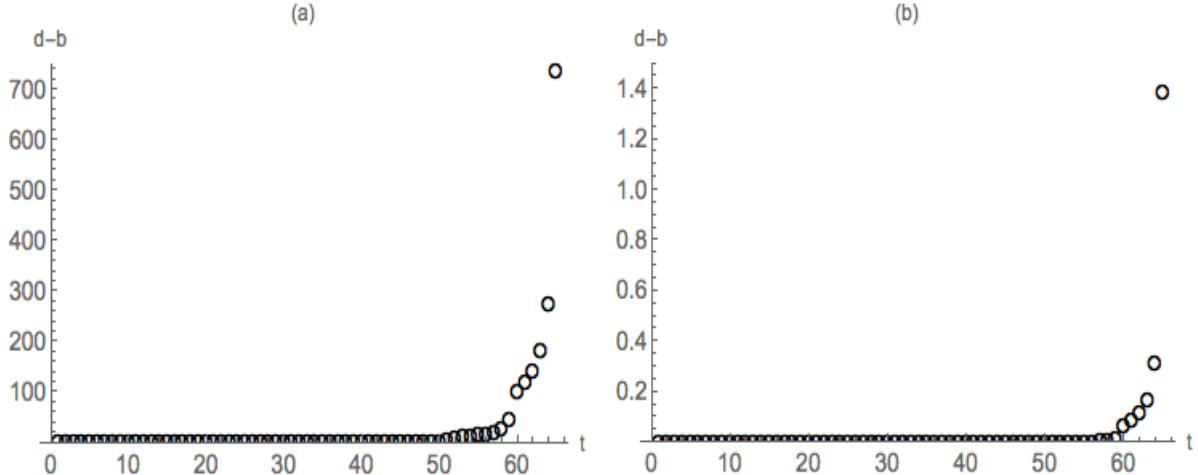


Figure 8: Lifespans  $d - b$  for (a)  $\beta_0$  and (b)  $\beta_1$  computed for  $100 \times 100$  triangulation

From Tables 3 and 4, we see that  $d_B = d_{W^1} = d_{W^2}$ . Thus, the samples agree that a single change in the geometry is occurring – with no small features contributing to changes in the geometry – and increases by several orders of magnitude from the beginning to the end of the evolution. The only differences between the respective measured distances in the  $50 \times 50$  and  $100 \times 100$  cases are

in the orders of their magnitudes. The points in adjacent diagrams are born at almost exactly the same value and die at almost exactly the same value until near the end of the evolution. Also, the distances between adjacent PD's change little until the final four time indices. So, this single effect occurs mainly at the end of the evolution. This can be attributed to the type of singularity formation for the symmetric dumbbell: the singularity forms at one location on the neck.

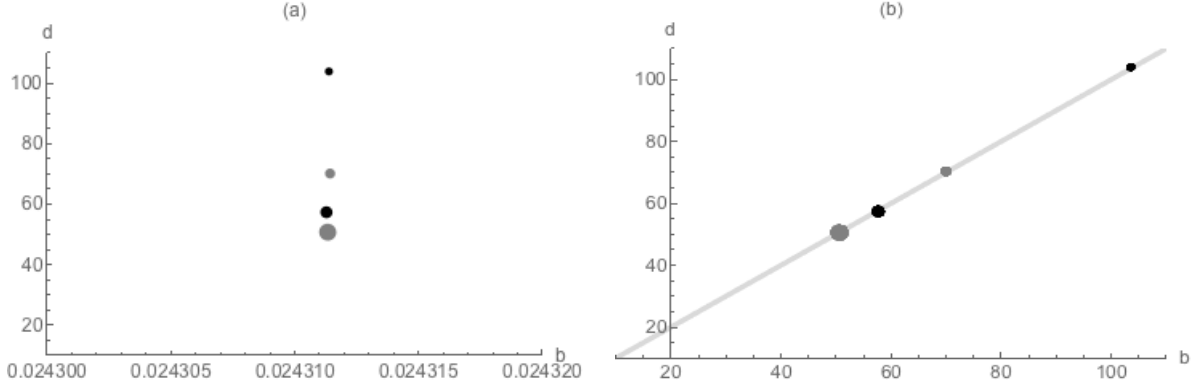


Figure 9:  $50 \times 50$  case: These are plots of the final four PD's, death vs. birth ( $d$  vs.  $b$ ), for the connected components (a) and the holes (b) represented in the table below where we list the bottleneck, Wasserstein-1, and Wasserstein-2 distances between adjacent diagrams. The sizes of the points in the plots decrease with increasing time index; the colors alternate between black and gray to distinguish the points further in the diagram. The light grey line is the set of points with equal birth and death values. Points related to infinite lifespans are omitted from the diagram.

$50 \times 50$	$\beta_0$	$\beta_1$
$(PD^i, PD^{i+1})$	$(d_B, d_{W1}, d_{W2})$	$(d_B, d_{W1}, d_{W2})$
$i = 1$	0	0
$i = 17$	$2 \times 10^{-5}$	$2 \times 10^{-5}$
$i = 33$	$1.46 \times 10^{-3}$	$1.46 \times 10^{-3}$
$i = 49$	$6.95 \times 10^{-1}$	$6.95 \times 10^{-1}$
$i = 61$	4.98	4.99
$i = 62$	7.09	7.10
$i = 63$	$1.23 \times 10^1$	$1.23 \times 10^1$
$i = 64$	$3.37 \times 10^1$	$3.38 \times 10^1$

Table 3: This table shows the bottleneck, Wasserstein-1, and Wasserstein-2 distances between the first two, middle two, and last two PD's associated with the connected components ( $\beta_0$ ) and holes ( $\beta_1$ ) for the  $50 \times 50$  symmetric dumbbell. There are 65 PD's.

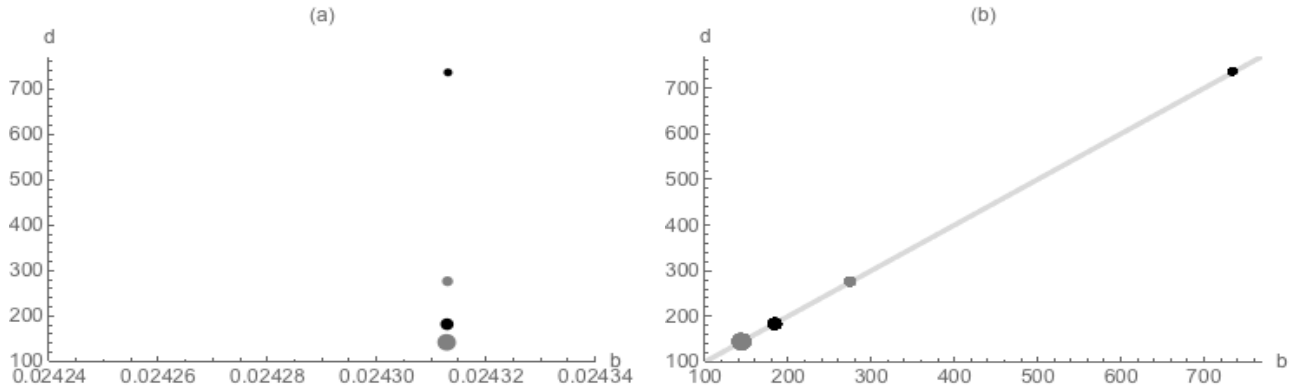


Figure 10:  $100 \times 100$  case: These are plots of the final four PD's, death vs. birth ( $d$  vs.  $b$ ), for the connected components (a) and the holes (b) represented in the table below where we list the bottleneck, Wasserstein–1, and Wasserstein–2 distances between adjacent diagrams. The sizes of the points in the plots decrease with increasing time index; the colors alternate between black and gray to distinguish the points further in the diagram. The light grey line is the set of points with equal birth and death values. Points related to infinite lifespans are omitted from the diagram.

$100 \times 100$	$\beta_0$	$\beta_1$
$(PD^i, PD^{i+1})$	$(d_B, d_{W1}, d_{W2})$	$(d_B, d_{W1}, d_{W2})$
$i = 1$	0	0
$i = 17$	$2 \times 10^{-5}$	$2 \times 10^{-5}$
$i = 33$	$1.58 \times 10^{-3}$	$1.58 \times 10^{-3}$
$i = 49$	$8.22 \times 10^{-1}$	$8.22 \times 10^{-1}$
$i = 61$	$2.45 \times 10^1$	$2.45 \times 10^1$
$i = 62$	$4.07 \times 10^1$	$4.07 \times 10^1$
$i = 63$	$9.01 \times 10^1$	$9.02 \times 10^1$
$i = 64$	$4.61 \times 10^2$	$4.62 \times 10^2$

Table 4: This table shows the bottleneck, Wasserstein–1, and Wasserstein–2 distances between the first two, middle two, and last two PD's associated with the connected components ( $\beta_0$ ) and holes ( $\beta_1$ ) for the  $100 \times 100$  symmetric dumbbell. There are 65 PD's.

#### 4.2.2 Dimpled Dumbbell

The dimpled dumbbell is featured below (Figure 11). The necks are at  $x = -180$ ,  $x = -66$ ,  $x = 0$ , and  $x = 130$ . The greatest pinching occurs at the neck  $x = 0$ , whose neck radius, from initial time index to final time index, decreases by three orders of magnitude. Also, the scalar curvature at this neck grows by seven orders of magnitude. The other necks demonstrate pinching but within one order of magnitude in both neck radius and scalar curvature. Most values of  $\psi$  remain constant across the evolution.

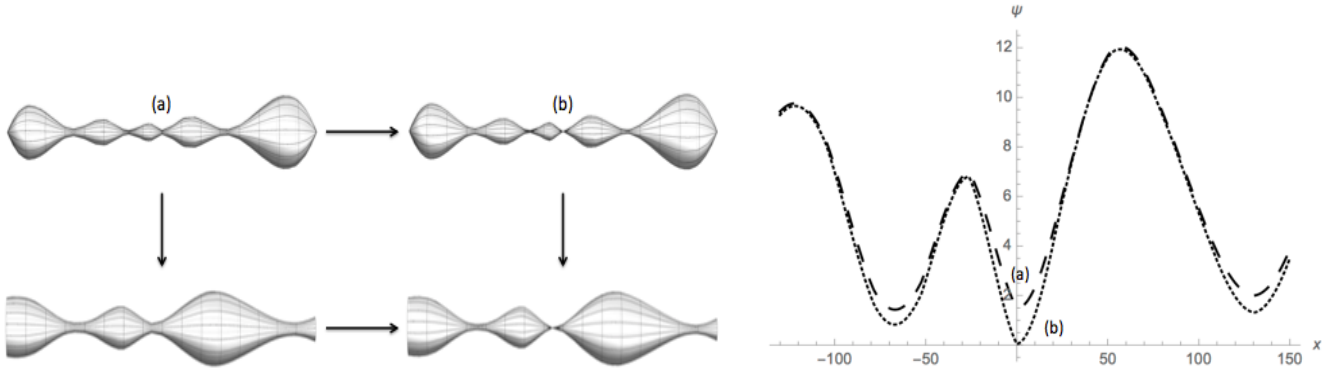


Figure 11: This is an illustration of the dimpled dumbbell. The three-dimensional surfaces (above) are the plots of the dumbbell on the interval  $[-100\pi + 0.1, 100\pi - 0.1]$  and close-ups of some of the necks – including the most-pinched neck – on the interval  $[-130, 150]$  at initial time  $t = 0$  (a) and final time  $t = 1.1599$  (b). The initial (long dash) and final (short dash) radial profiles are plotted below on the interval  $[-130, 150]$ .

The triangulation is on a  $50 \times 10$  grid for 70 time indices. The lifespans (Figure 12) resemble a hybrid between those of the dimpled sphere and those of the symmetric dumbbells. For the  $\beta_0$  tables, we have four finite lifespans and one infinite lifespan of low scalar curvature for all time indices. Two of the finite lifespans show a modest increase in birth value but two orders of magnitude increase in death value over the evolution of the object. The remaining finite lifespans show an order of magnitude increase from birth value to death value. Of these, one interval does not change much over the entire evolution, while the other changes but remains within the same order of magnitude. The  $\beta_1$  tables have lifespans of variously short lengths but no infinite ones. Though some of the lifespans grow to lengths similar to those in the  $\beta_0$  tables, they are of the same order of magnitude.

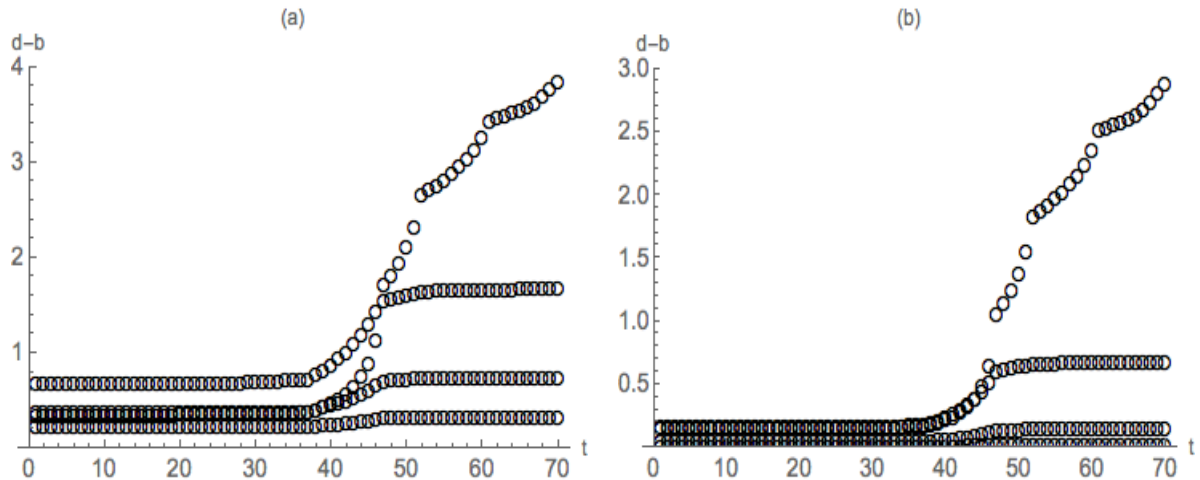


Figure 12: Lifespans  $d - b$  for (a)  $\beta_0$  and (b)  $\beta_1$  computed for  $50 \times 10$  triangulation

In looking at the distances between adjacent PD's (Table 5), we see that initially,  $d_{W^2}$  is much closer to  $d_B$  than it is to  $d_{W^1}$  (though all are within the same order of magnitude). This indicates that small changes in the geometry dominate differences in the PD's over a single large change. As the final time is approached, however,  $d_{W^1}$  is only slightly larger than  $d_{W^2}$  or  $d_B$  (which are almost identical). This indicates that a single large change dominates differences in the PD's. The genetically modified peanut shares features with the previous cases of the dimpled sphere and the symmetric dumbbell: small changes in the geometry initially dominate differences in the PD's while

a single large change leads to a neckpinch at the end of the evolution, the latter of which is expected from RF.

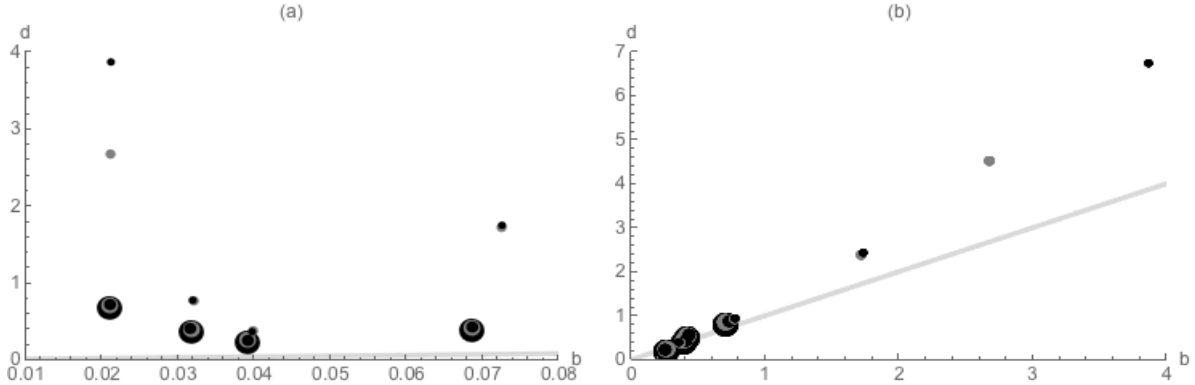


Figure 13: These are plots of the first and last PD's (and the PD's between them for the quartiles of data partitioned by time index), death vs. birth ( $d$  vs.  $b$ ), for the connected components (a) and holes (b) for the genetically modified peanut represented in the table below where we list the bottleneck, Wasserstein–1, and Wasserstein–2 distances between the adjacent diagrams. The sizes and colors of the points in the plots distinguish the time indices from which they come, with the sizes decreasing with increasing time indices and the colors alternating as some of the points are close. The light gray line is the set of points with equal birth and death values.

GMP $50 \times 10$	$\beta_0$	$\beta_1$
$(PD^i, PD^{i+1})$	$(d_B, d_{W1}, d_{W2})$	$(d_B, d_{W1}, d_{W2})$
$i = 1$	$(3 \times 10^{-6}, 8 \times 10^{-6}, 4.24 \times 10^{-6})$	$(5 \times 10^{-6}, 1.2 \times 10^{-5}, 6.78 \times 10^{-6})$
$i = 18$	$(3.8 \times 10^{-5}, 8.3 \times 10^{-5}, 4.76 \times 10^{-5})$	$(5.2 \times 10^{-5}, 1.13 \times 10^{-4}, 6.59 \times 10^{-5})$
$i = 35$	$(4.12 \times 10^{-3}, 9.03 \times 10^{-3}, 5.18 \times 10^{-3})$	$(5.7 \times 10^{-3}, 1.22 \times 10^{-2}, 7.25 \times 10^{-3})$
$i = 52$	$(4.72 \times 10^{-2}, 5.02 \times 10^{-2}, 4.73 \times 10^{-2})$	$(8.74 \times 10^{-2}, 6.61 \times 10^{-1}, 8.75 \times 10^{-2})$
$i = \max$	$(8.097 \times 10^{-2}, 8.15 \times 10^{-2}, 8.098 \times 10^{-2})$	$(1.53 \times 10^{-1}, 1.54 \times 10^{-1}, 1.53 \times 10^{-1})$

Table 5: This table shows the bottleneck, Wasserstein–1, and Wasserstein–2 distances between the first two and last two PD's associated with the connected components ( $\beta_0$ ) and holes ( $\beta_1$ ) for the genetically modified peanut (GMP). There are 70 PD's.

### 4.3 Degenerate Neckpinch

The case where  $\alpha = 0$  gives us an asymmetric dumbbell with a pinch on the right polar cap under RF ( $\epsilon = 0.001$  so that we come in by 0.1 unit before adjusting for equal function height to the left pole) in Figure 14. The right pole sees a decrease of two orders of magnitude, while the scalar curvature on this pole increases by three orders of magnitude. The rest of the plot is essentially static with little change in the values of  $\psi$ .

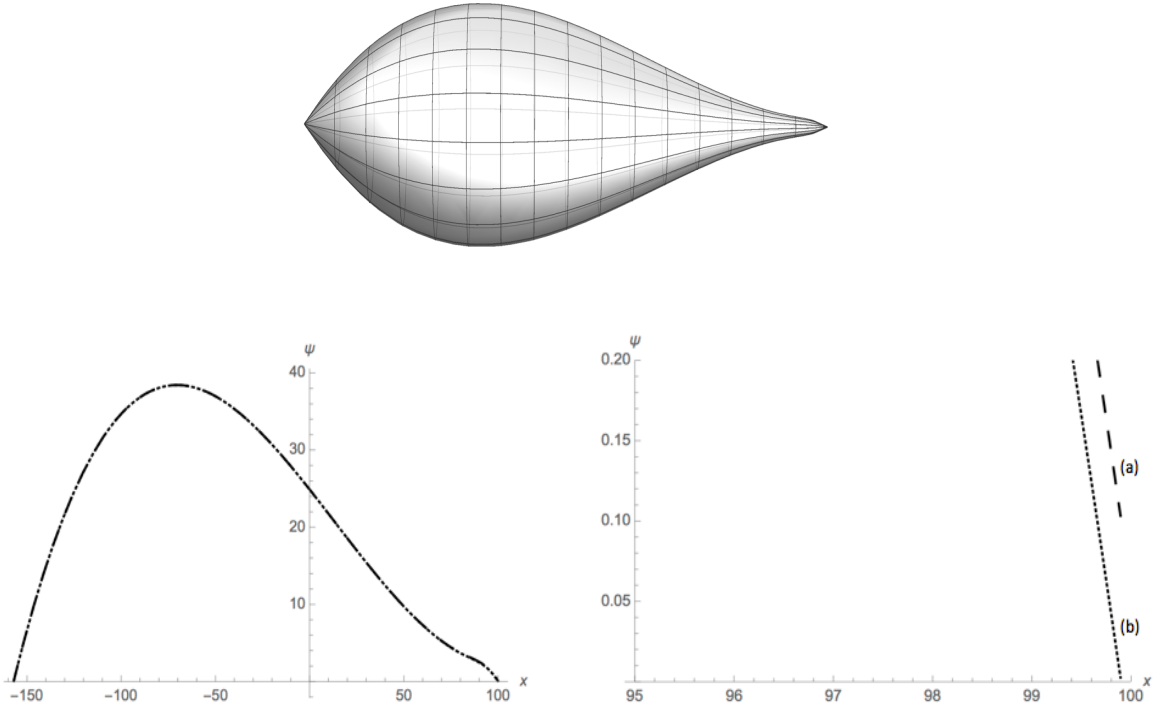


Figure 14: This is an illustration of the plots of the surface at initial time  $t = 0$  (a) and final time  $t = 0.206$  (b). The initial and final radial profiles, as well as a closeup of the right pole, is on the right.

Pinching is indicated by a high scalar curvature value on the right pole and the radii of the spheres in that region approaching zero with two orders of magnitude difference between the initial and final profile at the right pole. This contrasts with the radii on the left pole which are almost unchanged in the same time interval.

After reductions at each time index, we obtain only tables for connected components. In the **Perseus** output, we again see only a single infinite lifespan of a low scalar curvature value and a single connected component across all birth values of scalar curvature at each time index. The distances obtained from the first time index to the later time indices are all within  $10^{-6}$  of each other. As a collection of points, this is not surprising as the only changes across all time indices occur near the right pole, and these changes are not large or strikingly different. The topological signal here comes only from the infinite lifespans and indicates that a single change in the geometry – the neckpinch on the pole – drives differences in the PD’s.

## 5 Conclusions and Future Directions

The application of PH to RF provides a unique opportunity to analyze topologically a collection of data over which we have substantial command, in this case meaning that we have generated the data numerically and have a ready filtration (scalar curvature). This differs from what is usually encountered in problems of PH, where the assignment of a metric to the data or the choice of a filtration parameter to implement is unclear. We are able to compute scalar curvature at any point on our objects, at any time in the evolution. Given a sample of points, we then can construct a triangulation and assign the scalar curvature on edges as an average of scalar curvatures of endpoints sharing the edges. We find from these outputs that PH provides a topological characterization of the

formation and type of singularity produced under RF.

At each time step, looking at the outputs of **Perseus**, we find for the different models three classifications of lifespans: negligible finite, finite, and infinite. The tables for connected components display all of these classifications; those for the tunnels only have negligibly finite intervals. The first classification consists of extremely short intervals representing features that do not persist over many values of scalar curvature. The second classification consists of longer finite intervals, one or more orders of magnitude longer than the first class of finite intervals. The third classification consists of infinite persistence intervals associated to low values of scalar curvature. At each time index, as intervals are born, we see the birth of connected components. When these die, we see the birth of tunnels. As we filter over higher values of scalar curvature and look at the birth values of new cells, we see the disappearance or reappearance of certain features.

The dimpled 2-sphere uniformizes in curvature before collapsing to a point. The lifespans reflect this transition as most of the finite intervals vanish at the time of uniformization, returning only near the end of the evolution. Infinite intervals with increasing birth scalar curvature at each time step appear in the tables of persistence intervals for dimension 0.

At each time index, for the connected components, we have an infinite interval, a longer finite interval, and a number of shorter finite intervals. For the tunnels, we have a number of short finite intervals. This holds until time index 30000, where we have only a brief finite interval and an infinite interval for the connected components, and similarly brief finite intervals for the tunnels. After this time index, until the end, we see an increase in the number of short, finite intervals in both the tables for connected components and tunnels. At the final time index, we see an infinite interval and brief finite intervals for the connected components, as well as brief, finite components for the tunnels.

As a set of data points, the distances between PD's reveals that, as the evolution progresses, small features are usually dominant in changing the geometry. Once the object has attained uniform scalar curvature and starts to collapse, all of the data points converge to a common point. This corresponds with many small changes occurring and coincides with the formation of a singularity.

The symmetric dumbbell, at each time index for the connected components, has an infinite lifespan and one finite lifespan. For the tunnels, we have a number of brief, finite intervals. This is true for the different spatial resolutions, where only the individual birth and death values and the scale of their differences change. The distance measures between adjacent PD's are all the same; this indicates that only a single large feature changes the geometry. This single change manifests mainly at the end of the evolution and coincides with the formation of a neckpinch singularity.

The genetically modified peanut has, for the connected components at each time index, an infinite lifespan, between two and four brief finite lifespans, and two or more longer finite lifespans. As time progresses, one of these becomes much longer. For the tunnels, there are shorter and longer finite lifespans. Unlike the small-lobed dumbbell, we expect that we have more intervals because we have many more local extrema in the radii of the spheres comprising the dumbbell (hence more local extrema in the filtration parameter). The distances between the PD's initially indicate that small features dominate in changing the geometry. By the end of the evolution, the distance measures become much closer, indicating a single large effect changing the geometry. This coincides with a neckpinch singularity. In this way, the genetically modified peanut is a hybrid between the dimpled sphere and the symmetric dumbbell.

For the degenerate dumbbell, at each time index, there is only an infinite persistence interval in the tables for connected components. No tables for tunnels are generated: for all values of the filtration, there is only a single connected component. The distance measures between adjacent diagrams are the same, indicating the action of a single large effect on changes in the geometry. Between adjacent PD's, the distances are small; the formation of a singularity can be detected by looking at differences in distances between PD's at separated time indices, though the largest of these is around  $10^{-6}$ .

We conclude that the dominance of small or large features in changes to the geometry of an object depends on the type of object and the type of singularity it can manifest under RF. At different times in the evolution, small features or large features can dominate. For the four models we considered here, the topological signals are distinct.

For future work, we would like to use PH to investigate systems with incomplete or sparse data. This includes problems involving the interpretation of data for hard-to-compute higher-dimensional scenarios which may appear in the context of physical problems with more than 4 dimensions or systems with a large number of degrees of freedom (e.g., phase spaces). Another is to take sparse data, such as that obtained for density matrices, and consider different filtrations for filling in the missing data as in matrix imputation.

We are also interested in the use of PH and RF to explore quantum entanglement. The former would be able to investigate quantum entanglement via filtration over a function such as entropy [1], the tangle [10], or other invariants [27]. RF is understood on continuum manifolds both real and complex, and matrix product states (of which cluster states are) have recently been given a differential geometric representation [15].

Understanding of the global behavior of the data here is useful in approaching new problems that present computational challenges that defy well-developed methods but are amenable to topological techniques.

## 6 Acknowledgements

HAB acknowledges support from United States Air Force (USAF) Grant # FA8750-11-12-0275. MC would like to thank the University of Wisconsin-Stout Faculty Start-Up Fund and the National Academy of Sciences, National Research Council (NRC) Research Associateship program for support during this work. We would like to thank Rory Conboye for a careful reading of the manuscript and for sharpening the RF equation in 3-dimensions and Don Sheehy for helpful questions and remarks regarding this work. WAM would like to thank the Department of Mathematics at Harvard University for their support and hospitality, and especially S-T Yau for his valuable insights in this area. WAM also acknowledges support from United States Air Force (USAF) Grants # FA8750-11-2-0089 and # FA8750-15-2-0047, and support from the Air Force Research Laboratory/Trusted Systems Branch (AFRL/RITA) through the Visiting Faculty Research Program (VFRP) administered through the Griffiss Institute. KM would like to thank the National Science Foundation for grants NSF-DMS-0835621, 0915019, 1125174, 1248071, and contracts from Air Force Office of Scientific Research (AFOSR) and Defense Advanced Research Projects Agency (DARPA). VN is grateful to Robert Ghrist for insightful discussions. His work was funded in part by Defense Advanced Research Projects Agency grant DARPA DSO-FA9550-12-1-0416. Any opinions, findings, and conclusions or recommendations expressed in this material are those of the author(s) and do not necessarily reflect the views of the Air Force Research Laboratory.

## References

- [1] K. Anand & G. Bianconi, “Entropy measures for networks: Toward an information theory of complex topologies,” *Phys. Rev. E*, **80**, 045102(R) (2009)
- [2] S. Angenent, J. Isenberg, & D. Knopf, “Formal matched asymptotics for degenerate Ricci flow neckpinches,” *Nonlinearity* **24**, 2265–2280 (2011); “Degenerate neckpinches in Ricci flow,” *J. Reine Angew. Math. (Crelle)*, **709**, 81–118 (2015)

[3] S. Angenent & D. Knopf, “An example of neckpinching for Ricci flow on  $S^{n+1}$ ,” *Math. Res. Lett.*, **11**, No. 4, 493–518 (2004)

[4] R. L. Bishop & S. I. Goldberg, *Tensor Analysis on Manifolds*, Dover Publications, Inc., New York (1980)

[5] H-D. Cao, B. Chow, S-C Chu & S-T Yau, eds., *Collected Papers on Ricci Flow* in Series in Geometry and Topology, Vol. 37, International Press, Somerville, MA (2003)

[6] G. Carlsson, “Topology and Data,” *Bull. Amer. Math. Soc.*, **46**, No. 2, 255–308 (2009)

[7] F. Chazal, V. de Silva, M. Glisse, & S. Oupoint, “The structure and stability of persistence modules,” *arXiv:1207.3674* (2012)

[8] B. Chow, S-C Chu, D. Glickenstein, C. Guenther, J. Isenberg, T. Ivey, D. Knopf, P. Lu, F. Luo, & L. Ni, *The Ricci Flow: Techniques and Applications, Part 1: Geometric Aspects*, Mathematical Surveys and Monographs, Vol. 135, American Mathematical Society, Providence, RI (2007)

[9] B. Chow & D. Knopf, *The Ricci Flow: An Introduction*, Mathematical Surveys and Monographs, Vol. 110, American Mathematical Society, Providence, RI (2004)

[10] V. Coffman, J. Kundu, & W. K. Wootters, “Distributed Entanglement,” *Phys. Rev. A*, **61**, 052306 (2000)

[11] H. Edelsbrunner & J. Harer, “Persistent homology: A survey,” *Surveys on discrete and computational geometry*, 257–282, American Mathematical Society, Providence, RI (2008)

[12] H. Edelsbrunner & J. Harer, *Computational Topology*, American Mathematical Society, Providence, RI (2009)

[13] R. Ghrist, “Barcodes: the persistent topology of data”, *Bull. Amer. Math. Soc. (N.S.)*, **45**, No. 1, 61–75 (2008)

[14] H.-L. Gu & X.-P. Zhu, “The Existence of Type II Singularities for the Ricci Flow on  $S^{n+1}$ ,” *math.DG/0707.0033* (2007); D. Garfinkle & J. Isenberg, “The Modelling of Degenerate Neck Pinch Singularities in Ricci Flow by Bryant Solitons,” *math.DG/0709.0514* (2007)

[15] J. Haegeman, et al., “Geometry of matrix product states: Metric, parallel transport, and curvature,” *J. Math. Phys.*, **55**, 021902 (2014)

[16] R. S. Hamilton, “Three manifolds with positive Ricci curvature,” *J. Diff. Geom.*, **17**, 255–306 (1982)

[17] R. S. Hamilton, “The formation of singularities in the Ricci flow,” *Surveys in differential geometry, Vol. II*, 7–136, Internat. Press, Cambridge, MA (1995)

[18] T. Kaczynski, K. Mischaikow, & M. Mrozek, *Computational Homology*, Applied Mathematical Sciences, Vol. 157. Springer-Verlag, New York (2004)

[19] A. Goulet, M. Kramár, L. Kondic, & K. Mischaikow, “Evolution of Force Networks in Dense Particulate Media,” *Phys. Rev. E*, **90**, 052203, 5 (2014)

[20] W. A. Miller, P. M. Alsing, M. Corne, & S. Ray, “Equivalence of Ricci flow and Hamilton’s Ricci flow for 3D neckpinch geometries,” *Geom. Imag. Comp.*, **0**, No. 0, 1–34 (2014)

- [21] W. A. Miller, J. R. McDonald, P. M. Alsing, D. Gu, & S-T Yau, “Ricci flow,” *Comm. Math. Phys.*, **239**, No. 2, 579-608 (2014)
- [22] M. Nakahara, *Geometry, Topology, and Physics*, Institute of Physics Publishing, Philadelphia (2003)
- [23] V. Nanda, “Perseus: the Persistent Homology Software”, [www.sas.upenn.edu/~vnanda/perseus](http://www.sas.upenn.edu/~vnanda/perseus) (2012)
- [24] V. Nanda & R. Sazdanovic, “Simplicial Models and Topological Inference in Biological Systems,” in *Discrete and Topological Models in Molecular Biology*, eds. N. Jonoska and M. Saito, Springer-Verlag, Heidelberg (2014)
- [25] V. Robins, P. J. Wood, & A. P. Sheppard, “Theory and algorithms for constructing discrete Morse complexes from grayscale digital images”, *IEEE Transactions on Pattern Analysis and Machine Learning*, **33**, No. 08, 1646-1658 (2011)
- [26] W. Thurston, *Three-dimensional geometry and topology*, Vol. 1. Edited by Silvio Levy, Princeton Mathematical Series, 35, Princeton University Press, Princeton, NJ (1997)
- [27] S. N. Walck, J. K. Glasbrenner, M. H. Lochman, & S. A. Hilbert, “Topology of the three-qubit space of entanglement types,” *Phys. Rev. A*, **72**, 052324 (2005)
- [28] A. Zomorodian & G. Carlsson, “Computing persistent homology”, *Discrete Comput. Geom.*, **33**, 249-274 (2005)